Control Engineering Practice 160 (2025) 106318

Contents lists available at ScienceDirect

Control Engineering Practice

journal homepage: www.elsevier.com/locate/conengprac

A double-loop robust position and speed control of an electromagnetic actuator against nonlinear model uncertainties

Han-Sol Lee [a,b,#], Yeongoh Ko [a,#], Juhoon Back [c], Keum-Shik Hong [d,e], Chang-Sei Kim [a,*]

[a] School of Mechanical Engineering, Chonnam National University, Gwangju 61186, South Korea
[b] Center for Humanoid Research, Korea Institute of Science and Technology, Seoul 02792, South Korea
[c] School of Robotics, Kwangwoon University, Seoul 01897, South Korea
[d] School of Mechanical Engineering, Pusan National University, Pusan 46241, South Korea
[e] Institute for Future, School of Automation, Qingdao University, Qingdao 266071, China

ARTICLE INFO

Keywords:
Electromagnetic actuation
Microrobot
Sliding mode control
Disturbance observer
Robust control

ABSTRACT

Electromagnetic actuation (EMA) has been a reliable and powerful approach for the wireless manipulation of a small-sized robot in recent years. EMA with controllers for microrobot manipulation has been validated in various studies and demonstrated high precision in static environments. Nevertheless, from a control perspective, challenges remain in effectively compensating for lumped disturbances, which include nonlinear model uncertainties and unpredictable dynamics of target objects, thereby ensuring reliable performance in practical applications. In this article, we propose a double-loop robust controller to address these challenges. The proposed control architecture consists of an outer-loop sliding mode control (SMC) and an inner-loop disturbance observer (DOB). This controller functions as a force compensator, where the SMC provides primary feedback control for the motion of the magnetic object, and the DOB estimates and compensates for lumped disturbance forces. The controller's parameters and driving performance were comprehensively analyzed through dynamic simulations of the target object. The potential for practical applications was validated through experiments. The results demonstrated that position control accuracy reached 0.4 mm at a rated speed within 1 mm/s, showing a 71 % improvement compared to conventional control. Additionally, the comparative speed control performance could achieve a maximum speed of 11.4 mm/s resulting in relative effectiveness compared to other control approaches.

1. Introduction

Magnetic actuation technology is a promising strategy for achieving wireless control of the direction and movement of magnetic microrobots (Wang et al., 2023a, b). Among various actuation methods, such as optical, chemical, and biological approaches, electromagnetic actuation (EMA) has proven to be an effective and versatile solution. It enables multi-degree-of-freedom (DOF) motion of magnetic objects by precisely regulating magnetic force and torque through the coordinated control of multiple electromagnet coils (Yang & Zhang, 2020). Furthermore, as an intrinsic physical phenomenon, magnetic fields possess several advantageous characteristics, including the ability to permeate non-magnetic objects, high operational stability, and practical applicability. Leveraging these benefits, recent research has focused on developing advanced EMA systems with enhanced control techniques, thus broadening their applications in biomedical fields, such as micromanipulation, targeted drug delivery, and noninvasive or minimally invasive therapies.

Various EMA applications have leveraged both magnetic force and magnetic torque through magnetic field control. Rotating and oscillating magnetic fields have been used to drive and aggregate magnetic nanoparticles by concentrating magnetic fields in specific regions, showcasing their potential in targeted drug delivery and biosensor applications (Gharamaleki et al., 2024; Nguyen et al., 2021). Additionally, rotating magnetic fields have been applied to induce the deformation of microrobots, enabling crawling and walking motions that enhance their mobility in various environments (Hu et al., 2018;Lu et al., 2018). Magnetic force has been used to induce the movement of magnetic nanoparticles in fluids (Go et al., 2020; Law et al., 2024) and to control the movement of magnetic capsule endoscopes in the

* Corresponding author.
E-mail address: ckim@jnu.ac.kr (C.-S. Kim).
# These authors contributed equally to this work.

https://doi.org/10.1016/j.conengprac.2025.106318
Received 29 November 2024; Received in revised form 29 January 2025; Accepted 6 March 2025
Available online 22 March 2025

gastrointestinal (GI) tract (Huang et al., 2024; Song et al., 2022). Magnetic torque, determined by the magnetization direction of the magnetic robot relative to the magnetic field, has been employed to achieve rotational motion. For example, magnetic torque has been used to control the orientation of a magnetic capsule endoscope, enabling navigation through a wide range of GI tracts (Peker et al., 2024; Zhang et al., 2024), and magnetic guidewires have been steered through narrow blood vessels faster than with manual control (Gervasoni et al., 2024).

To realize these applications, EMA systems typically adopt a linearized control model based on two assumptions: a proportional relationship between input current and magnetic flux density, and the superposition property of the magnetic field (Chen et al., 2021; Ko et al., 2024). Here, the general magnetic field model is a function of position and current, which can be derived through mathematical modeling, finite element simulation, or actual measurements. The input current to each coil is then computed using a simplified mathematical model based on the traditional Biot–Savart law (Griffiths, 2017), reducing computation time and ensuring real-time system performance. These models show high agreement with actual systems and have been verified in various EMA applications (Cai et al., 2024).

However, EMA systems exhibit inherent nonlinear characteristics, leading to significant model uncertainties due to both internal and external disturbances. For example, inserting a core with hysteresis inside the electromagnet to enhance magnetic field generation significantly increases the model's nonlinearity. In this case, relying on linear models can result in performance degradation, affecting both accuracy and stability. Some studies have proposed generating a magnetic field map using measured datasets from a hall sensor and a tesla meter to form a desired magnetic field and force, even in regions where the core is saturated, and the current and magnetic field behave nonlinearly (Ongaro et al., 2019; Sikorski et al., 2019). However, finding a solution for inverse computation to calculate the required input current for each coil remains challenging. Additionally, the working environment is subject to unexpected disturbances from the external environment or inaccurate model parameters, such as incorrect Reynolds numbers due to turbulent flow in the medium and uncertainties in the drag coefficient as speed changes (Bailey, 1974). Therefore, a robust controller is necessary to address these challenges in the EMA system.

Several output feedback control approaches have been proposed EMA systems addressing magnetic field nonlinearity and uncertainty. The conventional proportional-integral-derivative (PID) controller is a representative example and has demonstrated effective driving performance through a simple control scheme (Go et al., 2020; Li et al., 2020). However, it has limitations, such as inappropriate compensation for external disturbances and system uncertainties. Additionally, significant efforts are required for tuning PID gains to control a wide range of speeds. H_∞ control, with a system matrix that quantifies the uncertainty in the force generation, was proposed to handle these issues (Marino et al., 2014). This approach, based on estimated EMA uncertainty, achieved stable control but incurred high computing costs due to the iterative nature of the H_∞ algorithm. Yang et al. (2021) addressed disturbance and uncertainties by combining disturbance observer (DOB) and fuzzy logic, but, the creation of fuzzy logic rules and the gain tuning were time-consuming. A nonlinear high-gain observer was proposed to estimate the microrobot's velocity and reduce measurement noise, enabling precise 3D motion (Ma et al., 2017). Lu et al. (2022), utilized an extended state observer (ESO) and sliding mode control (SMC) to estimate disturbances and perform tracking control. However, the nonlinear observers or ESOs have complex structures and require numerous tuning gains, while SMC may encounter chattering issues. Most previous robust controllers for EMA have focused primarily on output performance under specific conditions. However, these approaches lack sufficient analysis and experimental verification to identify the correlation between design parameters and system output. Additionally, these studies have been mostly limited to position control, with little attention given to controlling a range of speeds.

In this article, we propose a double-loop robust controller combining DOB and SMC to address the challenges of both position and speed control in EMA systems. The controller features SMC in the outer-loop and DOB in the inner-loop, which helps control the system output in a manner similar to the nominal system, without disturbance. This structure enables compensation for errors that arise when using traditional DOB or SMC individually. The DOB is a well-established control scheme, with numerous successful applications demonstrating its effectiveness in estimating lumped disturbances, including external factors and model uncertainties (Fu et al., 2023; Hashemi et al., 2022). Particularly, DOB exhibits good compatibility with other controllers when integrated into the inner-loop, without compromising the main controller's functionality. On the other hand, SMC is effective at compensating for disturbances when the difference between the real system and the model is known while ensuring robust nonlinear control performance (Mechali et al., 2022; Ovalle et al., 2019). The double-loop controller, combining these two approaches, offers the advantage of distributing the estimated disturbance value to a single operator, improving control precision and mitigating input signal chattering caused by high operating gains (Chen et al., 2023; Zhong et al., 2023). As a result, a well-tuned controller can enhance the controllability of objects with high dynamic characteristics, particularly for both position and speed control of EMA.

The main contributions and advancements of this work are summarized as:

1) We propose a novel EMA controller that integrates SMC and DOB to effectively compensate for both the nonlinearity and uncertainty in the EMA system and electromagnetic fields. Nonlinear model uncertainties, considered as lumped disturbances caused by model mismatches, are mitigated through the proposed double-loop robust control. The effectiveness of the controller is demonstrated by improved motion control of a magnetic object.
2) We present a detailed analysis and stability proof of a DOB-based SMC controller, which has not yet been applied to electromagnetic actuators despite its known robustness. The influence of key design parameters on system performance is thoroughly examined through simulations, providing practical design guidelines for robust EMA control.
3) A speed and position control approach for EMA is introduced, with a focus on dynamic performance across various speed ranges. The effectiveness of the proposed controller in handling varying speeds is validated through experiments. Additionally, the speed control performance of the controller is further verified through a comparative analysis.

To realize and validate the proposed methods, a control framework is designed based on the dynamics of a magnetic object in a state space and a conventional linear magnetic field model that is practically implemented in an actual 6-coil EMA system. Through the simulation, the generated magnetic field of the system is analyzed by the finite element method, and the effect of the individual actuators (SMC and DOB) is confirmed in the time and frequency responses. Especially, the enhanced position/speed control performance of a magnetic object can be achieved by the proposed double-loop control for the first time. Speed control performance in several micrometers per second while path tracking control has been reported through many studies (Ma et al., 2017; Ongaro et al., 2019), and control in an environment with flow velocity has also been recently published (Cao et al., 2022; Nguyen et al., 2021). However, there are still no reports studying the possibilities and limitations of high-speed control of objects with each of the proposed controllers. Subsequently, the contribution of the proposed controller was evaluated through two experiments demonstrating tracking motion control and speed control performance.

The remainder of this article is organized as follows. In Section 2, we

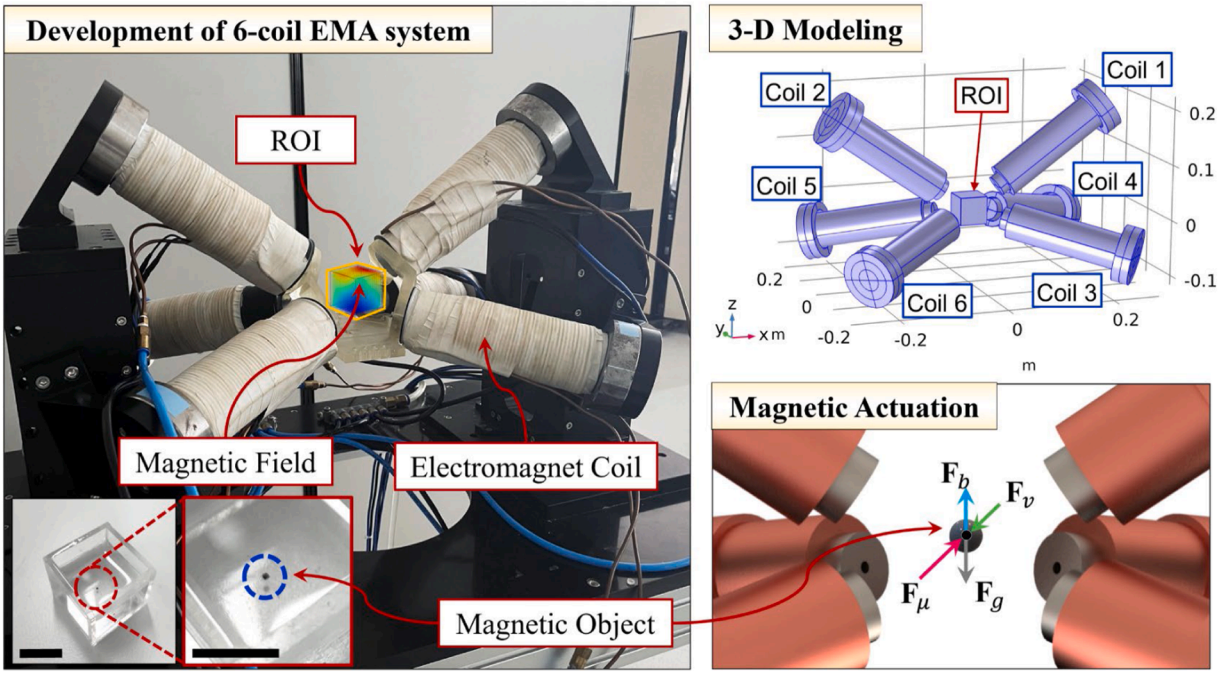

Fig. 1. System overview (6-coil EMA system). Yellow box is a region of interest (ROI), which is positioned at the center of the system. *Top-right inset*: Three-dimensional (3-D) modeling of the 6-coil system for numerical simulation. *Bottom-right inset*: Dynamic model of the magnetically actuated object in a viscous fluid. F_μ is the magnetic force, F_v is the drag force, F_b is the buoyancy, and F_g is the gravitational force. *Bottom-left inset*: Blue dashed line is a magnetic object used in this paper (Scale bar: 10 mm).

introduce the preliminaries and formulate the problems of existing EMA systems to achieve the desired goal. In Section 3, we present a robust double-loop controller for estimating and compensating for lumped disturbances combined with nonlinear model uncertainties of EMA systems. Then, we analyze the stability of the controller in terms of the designed parameters. In Section 4, simulations are performed to derive a correlation among control design parameters, stability, and control performance. Position and speed control performance validations through experiments are presented in Section 5. Conclusions and discussions for future work are given in Section 6.

2. Preliminaries and problem formulation

2.1. System configuration and characterization

This subsection introduces the overall EMA system configuration for control applications and explores the systemic characteristics of the magnetic field that cause nonlinearity and uncertainty issues in the EMA control. The EMA system used in this study consists of six core-filled coils, as shown in Fig. 1. The specifications of each electromagnet coil were the same: the outer diameter is 65 mm, the inner diameter is 45 mm, and the length of the electromagnet coil is 220 mm. The number of turns in each coil is 959 and it is wounded with copper wire with a diameter of 1.6 mm. Inside each coil, a pure iron core with a diameter of 40 mm and length of 250 mm was inserted. The overall frame of the presented EMA system was designed to create about $25 \times 25 \times 25$ mm^3 sized ROI at the center of each coil array.

A finite element analysis (FEA) was conducted to characterize the magnetic field in this system. A 3-D numerical model was developed in the COMSOL Multiphysics software (see Fig. 1), and the magnetic field simulations were performed. In particular, the applied currents were derived based on the relationship between magnetic field and current which is introduced in subSection 2.2. Fig. 2 presents the results of the magnetic field simulations in the designed ROI (as shown in Fig. 1), demonstrating the feasibility of controlling the field quantities (e.g., intensity, direction, and gradient). Although the desired magnetic field intensity and direction were set as constant values, spatial variances were observed (see Fig. 2(a)). This observation indicates that, even under constant input conditions, positional dependencies of the magnetic field may result in discrepancies between the modeled and actual magnetic forces acting on the target object.

Furthermore, Fig. 2(b) illustrates the nonlinear properties arising from the inserted iron core. As the applied current increases, the magnetic flux density exhibits saturation behavior in specific regions, causing the differences between the actual system and the model to become more pronounced. Additionally, external factors such as coil temperature, working medium properties, power source specifications, and energy transient response can introduce unpredictable discrepancies in the model. These characteristics provide crucial insights into the inherent nonlinearities and uncertainties of the EMA system. Based on this analysis, the following section presents a general modeling framework for EMA, laying the foundation for further investigation.

2.2. Dynamic model of magnetic objects in EMA

A conventional EMA model is formulated using a dynamic model of a magnetic object and external magnetic interaction torque $\tau_\mu \in \mathbb{R}^3$ and force $F_\mu \in \mathbb{R}^3$. The mathematical model of EMA can be described as the following form:

$$\begin{bmatrix} J\ddot{\theta} \\ m\ddot{x} \end{bmatrix} = \begin{bmatrix} \tau_\mu + \tau_v \\ F_\mu + F_v + F_b + F_g \end{bmatrix} \tag{1}$$

where $J \in \mathbb{R}^{3\times 3}$ is the moment of inertia, m is the mass of the magnetic object, and $\theta \in \mathbb{R}^3$ and $x \in \mathbb{R}^3$ represent the orientation and position of the magnetic object. The magnetic torque and force are defined as $\tau_\mu = V_o \mu \times B$ and $F_\mu = V_o(\mu \cdot \nabla)B$ (Kummer et al., 2010), where V_o is the volume of the object, $\mu \in \mathbb{R}^3$ is the magnetization vector of the magnetic object, and $B \in \mathbb{R}^3$ is the magnetic flux density. $\tau_v \in \mathbb{R}^3$ and $F_v \in \mathbb{R}^3$ are the drag torque and force, $F_b \in \mathbb{R}^3$ is the buoyant force, and $F_g \in \mathbb{R}^3$ is the gravitational force.

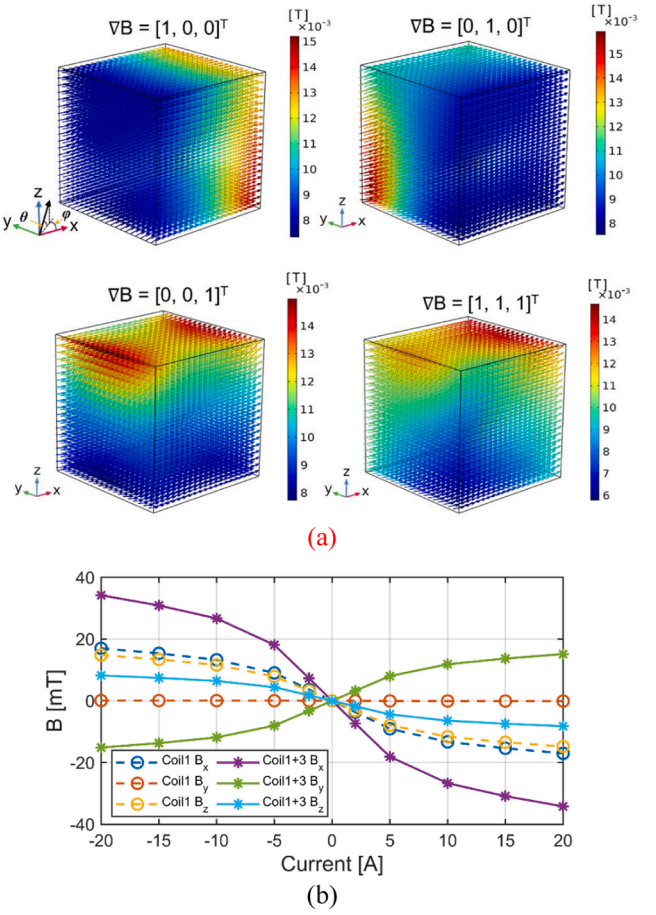

Fig. 2. Magnetic field simulation. (a) The result of magnetic field generated based on the input magnetic field intensity 0.01 T and gradient 0.1 T/m. ∇B denotes the gradient field direction vector. (b) Magnetic flux density at the center of the ROI as a function of current for one- or two-coil operation.

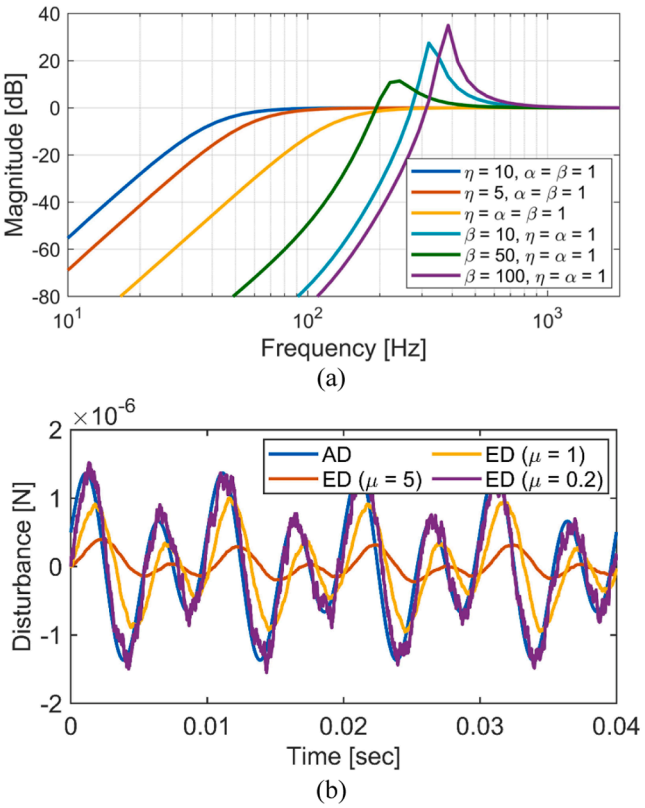

Fig. 4. Simulation results of the DOB. (a) Sensitivity function of the proposed DOB under different observer parameters. (b) Disturbance estimation result with the variation of parameter η. AD is the actual disturbance, and ED is the estimated disturbance.

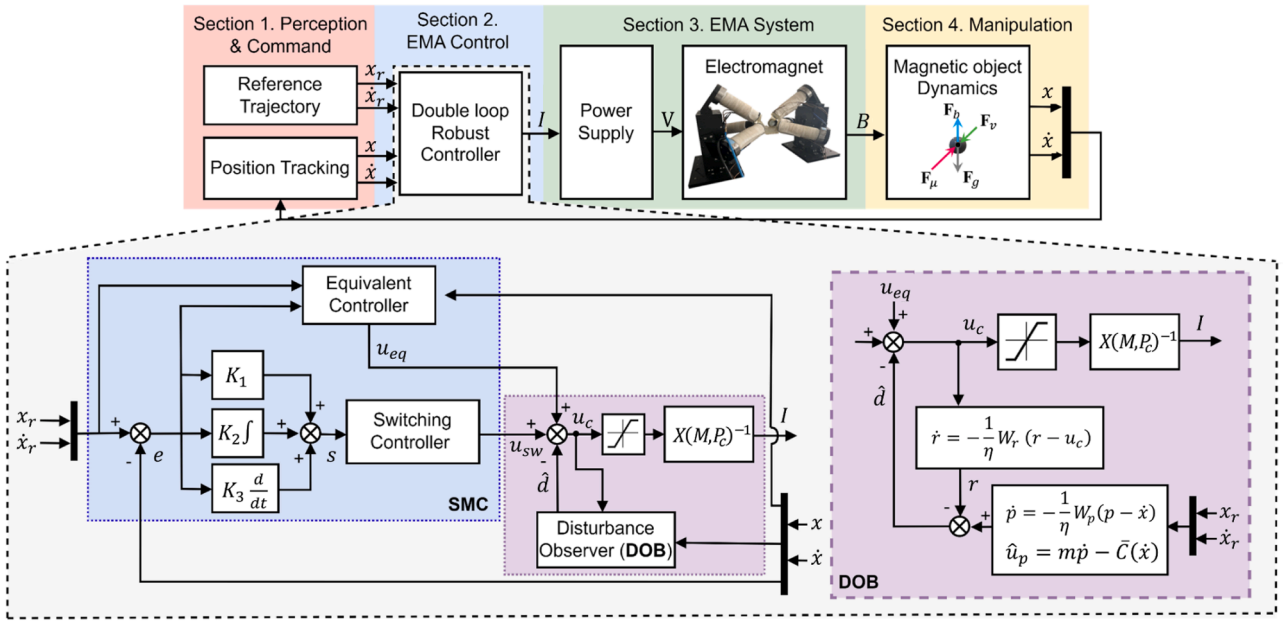

Fig. 3. Block diagram of the overall system and proposed double-loop robust controller. The blue dashed box indicates the sliding mode control law for the outer-loop, and the purple dashed box indicates the DOB operator for the inner-loop in the controller. *Note that the saturation function is inserted before current derivation to prevent excessive current application.*

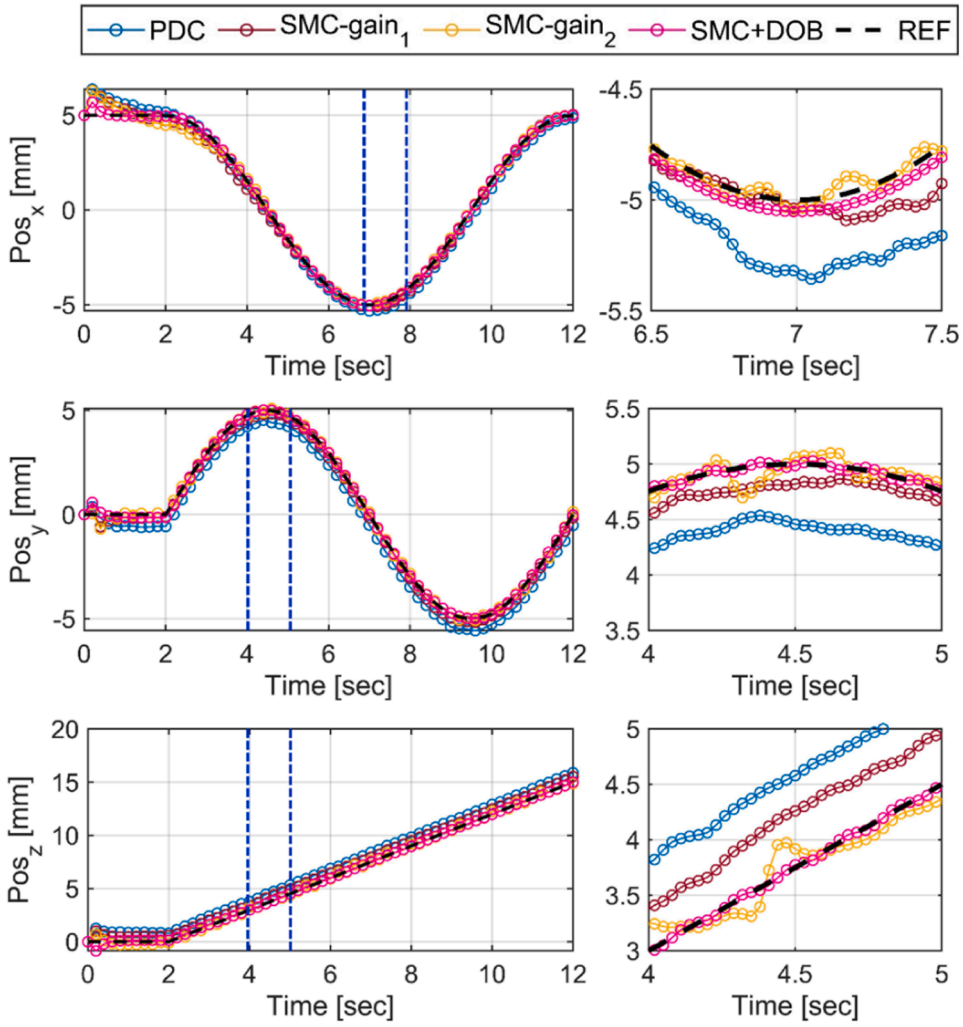

Fig. 5. Simulation results of the path-tracking control. Pos is the position of the object. The figures on the right show values for the blue dotted sections.

2.3. EMA model

The magnetic flux density B is proportionally related to the applied current i through the coil, i.e., $B \approx \widetilde{B}i$, where $\widetilde{B} \in \mathbb{R}^3$ is a proportional coefficient vector. This approximation is available when the magnetic field is generated by a low current within the ROI, and has been validated in previous studies (Kummer et al., 2010).

Accordingly, we can obtain the magnetic flux density B and the gradient ∇B as follows:

$$\begin{bmatrix} B \\ \nabla B \end{bmatrix} = \begin{bmatrix} \widetilde{B}_1(P) & \cdots & \widetilde{B}_n(P) \\ \dfrac{\partial \widetilde{B}_1(P)}{\partial j} & \cdots & \dfrac{\partial \widetilde{B}_n(P)}{\partial j} \end{bmatrix} \begin{bmatrix} i_1 \\ \vdots \\ i_n \end{bmatrix} = \begin{bmatrix} \mathscr{B}(P) \\ \dfrac{\partial \mathscr{B}(P)}{\partial j} \end{bmatrix} I \tag{2}$$

where $\mathscr{B}(P) \in \mathbb{R}^{3 \times n}$ and $\partial \mathscr{B}(P)/\partial j \in \mathbb{R}^{3 \times n}$, with $j \in \{x, y, z\}$, represent the unit matrix of the magnetic flux density and its gradient at a given position $P \in \mathbb{R}^3$, respectively. Additionally, $I \in \mathbb{R}^n$ is the current input vector in the n-coil EMA system. Then, by using the linear relation in Eq. (2), the magnetic torque and force can be expressed as

$$\begin{bmatrix} \tau_\mu \\ F_\mu \end{bmatrix} = V_o \begin{bmatrix} Sk(\mu)\mathscr{B}(P) \\ \mu \dfrac{\partial \mathscr{B}(P)}{\partial j} \end{bmatrix} I \tag{3}$$

where $Sk(\mu) = \begin{bmatrix} 0 & -\mu_z & \mu_y \\ \mu_z & 0 & -\mu_x \\ -\mu_y & \mu_x & 0 \end{bmatrix}$ is the skew-symmetric matrix of μ replacing the vector cross product between μ and $\mathscr{B}(P)$. In the case of the micro-scale object moving in a fluid medium, the control strategy can be simplified by first aligning the orientation through magnetic field control, rather than directly controlling the magnetic torque. Then, a simplified model is given by

$$\begin{bmatrix} B \\ F_\mu \end{bmatrix} = \begin{bmatrix} \mathscr{B}(P) \\ V_o \mu \dfrac{\partial \mathscr{B}(P)}{\partial j} \end{bmatrix} I = X(\mu, P) I \tag{4}$$

where $X(\mu, P) \in \mathbb{R}^{6 \times n}$ is the transformation matrix at unit current, which transforms the currents into the magnetic field and force. Finally, the current to generate the desired magnetic quantities is computed as follows:

$$I = X(\mu, P)^{\dagger} u_c \tag{5}$$

where $X(\mu, P)^{\dagger}$ is the pseudoinverse of matrix $X(\mu, P)$ and $u_c = [B_{des}; F_{\mu,\, des}] \in \mathbb{R}^6$ denotes the desired magnetic field and force vector (which corresponds to the control input).

To simplify the computational complexity in the modeling process, the unit transformation matrix $X(\mu, P_c)$ is generally applied at the center of the ROI, P_c. This approach assumes that the magnetic flux density errors at P_c and any position P within the ROI are allowable for feedback control system (Lee et al., 2024).

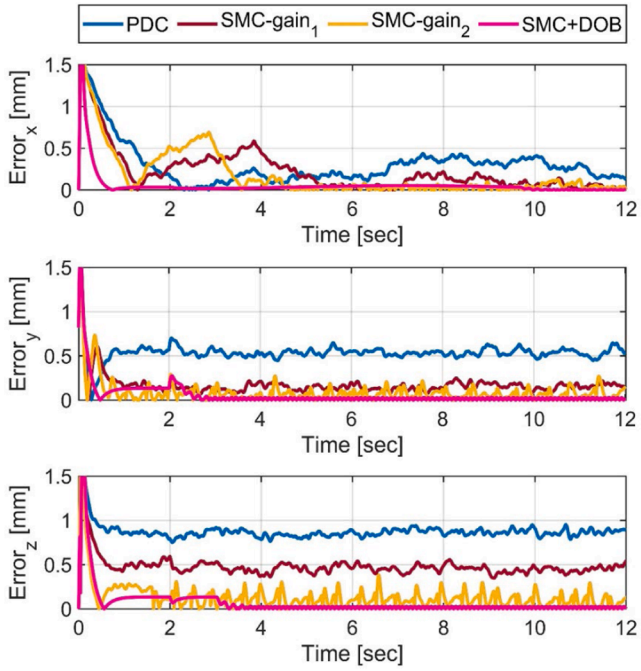

Fig. 6. Absolute value of errors in simulation results.

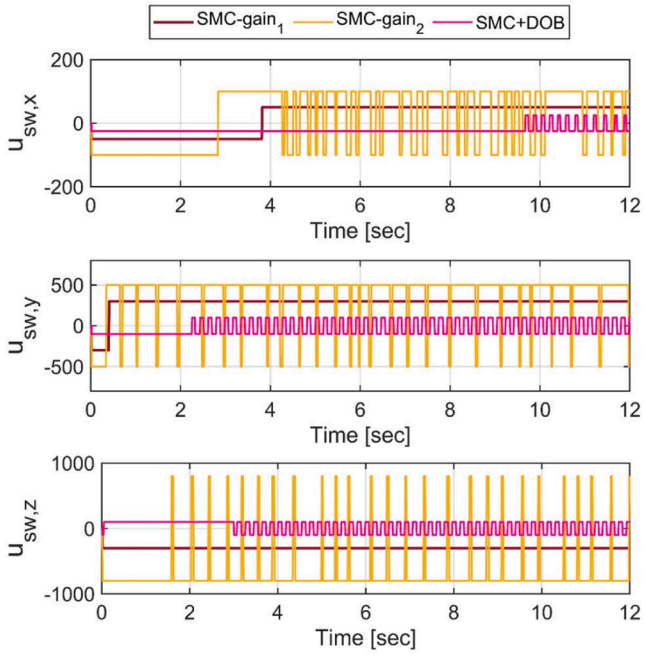

Fig. 7. Switching input of the helical trajectory motion control simulation.

2.4. Problem formulation

Based on the conventional EMA model and force-dominant dynamics, we redefined the model of the magnetic object. Thus, the dynamic model can be expressed as follows:

$$m\ddot{x} = F_\mu + F_v + F_b + F_g = C(\dot{x}) + u_c + F_d \tag{6}$$

where the uncertain force term is simplified as $C(\dot{x}) = F_v + F_b + F_g$, where $F_v = -0.5\rho_m A C_D v \| v \|$, $F_b = gV_o\rho_m$, $F_g = -mg$. Here, ρ_m is the medium density, A is the cross-sectional area of the moving object, C_D is the drag coefficient of the medium, v is the relative velocity between the object and fluid, and g is the gravitational acceleration. The magnetic force F_μ is replaced to $F_\mu = u_c + F_d$, where $u_c \in \mathbb{R}^3$ is a control input and $F_d \in \mathbb{R}^3$ is a bounded disturbance force.

The final goal of this work is to design a double-loop robust controller for a conventional EMA system such that the system output $x(t)$ converges to the reference trajectory, $x_r(t)$, i.e., for any given $\varepsilon > 0$, $\forall t \geq 0$, the system output and reference trajectory satisfy the following conditions:

$$\limsup_{t\to\infty} \| x_r(t) - x(t) \| \leq \varepsilon \tag{7}$$

From a practical perspective, a conventional controller (e.g., PID controller) can achieve significant performance when controllable conditions are held: the side effects from undesired magnetic quantities are negligible; there are no heating issues; and target object maintains slow dynamics during the task. However, since the conventional controller does not compensate for the disturbance force F_d, it is limited in achieving the high-level performance. Specifically, unmodeled factors can lead to performance degradation. Therefore, the proposed controller aims to make the actual system behave like an undisturbed nominal system at any given conditions, which is expressed below:

$$m\ddot{\bar{x}} = \bar{C}(\dot{\bar{x}}) + u_r \text{ with } [\bar{x}(0); \dot{\bar{x}}(0)] = [x(0); \dot{x}(0)] \tag{8}$$

where $\ddot{\bar{x}}$ and $\bar{C}(\dot{\bar{x}})$ denotes the nominal counterpart of $\ddot{x}$ and $C(\dot{x})$ composed of the known variables, respectively, and u_r is the outer-loop control input. Considering Eq. (6) and Eq. (8), a lumped disturbance $d \in \mathbb{R}^3$ is given as

$$d = F_d - \bar{C}(\dot{\bar{x}}) + C(\dot{x}) + m(\ddot{\bar{x}} - \ddot{x}) \tag{9}$$

Here, d includes not only the differences between the nominal and actual models, but also practical uncertainties such as hardware constraints, material properties, and unmodeled dynamics during operation, including environmental effects. For practical application, it is assumed that d and its time derivative are bounded, i.e., there exists $d^+ > 0$ such that the vector $[d(t); \dot{d}(t)]$ satisfies $\| d(t) \| \leq d^+$, $\forall t \geq 0$. Under this condition, the DOB and feedback control system can adequately estimate and compensate for d within the allowable DOB's bandwidth (Ha & Back, 2018).

The control input is constructed as $u_c = -\hat{d} + u_r$, where $\hat{d}$ is an estimate of the lumped disturbance d. In this work, u_r and $\hat{d}$ are designed using SMC law and the DOB in the outer and inner-loop, respectively. Finally, the control input u_c works as a force compensator, driving the original system Eq. (6) to behave like the undisturbed nominal system Eq. (8), such that the system output will satisfy condition Eq. (7).

3. Controller design

In this section, a DOB-based SMC is designed to address model uncertainties. The overall control structure in this study is shown in Fig. 3.

3.1. DOB design

$$m\ddot{x} = \bar{C}(\dot{x}) + u_c + d \tag{10}$$

We briefly describe the design of a DOB with two low-pass filters (LPFs) in the state space. The dynamic system in Eq. (6) is rearranged using the lumped disturbance Eq. (9) as follows:

Here, the signal $\ddot{x}$ is not measurable in this system; therefore, we employ a LPF to replace it with the signal $p \in \mathbb{R}^3$ as shown below:

$$\dot{p} = -\frac{1}{\eta} W_p (p - \dot{x}) \text{ with } p(0) = \dot{x}(0) \tag{11}$$

where η is a positive scalar gain related to the bandwidth of the LPF,

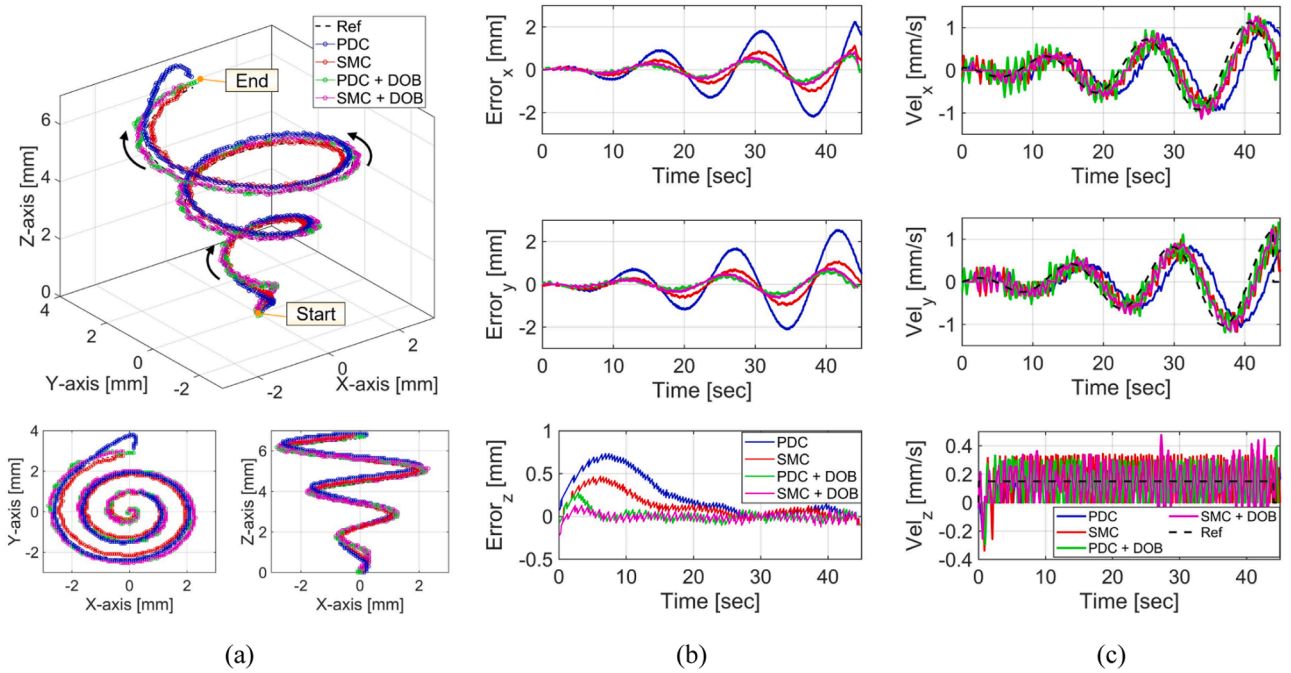

Fig. 8. Experimental results for motion control along a 3D trajectory using different controllers. (a) Tracking results of a magnetic object, (b) tracked position error, and (c) measured velocity for each axis.

Table 1
Comparison of the tracking control performance.

Controller	PDC	SMC	PDC + DOB	SMC + DOB
RMSE [mm]	1.38	0.66	0.39	0.40
STD [mm]	0.05	0.03	0.02	0.02

and $W_p = \mathrm{diag}(\alpha_j) \in \mathbb{R}^{3\times 3}$, with $\alpha_j \in \mathbb{R}^+$, is a positive definite diagonal matrix representing the LPF parameter, where $j \in \{x,\ y,\ z\}$. Then, $\hat{u}_p \in \mathbb{R}^3$, an estimate of $u_c + d$, is designed as

$$\hat{u}_p = m\dot{p} - \overline{C}(\dot{x}) \tag{12}$$

For estimating the lumped disturbance $\hat{d}$, a second LPF is constructed to replace u_c to r as follows:

$$\dot{r} = -\frac{1}{\eta} W_r (r - u_c) \tag{13}$$

where $W_r = \mathrm{diag}\left(\beta_j\right) \in \mathbb{R}^{3\times 3}$ with $\beta_j \in \mathbb{R}^+$ is a positive definite diagonal matrix representing the observer gain, $j \in \{x,\ y,\ z\}$. Using Eqs. (11)-(13), the estimate of $\hat{d}$ can be designed as

$$\begin{aligned} \hat{d} &= \hat{u}_p - r \\ &= m\left(-\frac{1}{\eta} W_p (p - \dot{x})\right) - \overline{C}(\dot{x}) - r \end{aligned} \tag{14}$$

The final control input force is computed as

$$\begin{aligned} u_c &= -\hat{d} + u_r \\ &= m\left(\frac{1}{\eta} W_p (p - \dot{x})\right) + r + \overline{C}(\dot{x}) + u_r \end{aligned} \tag{15}$$

where $u_r \in \mathbb{R}^3$ is the outer-loop control input.

3.2. SMC design

SMC is an advanced controller used to compensate for the distur-

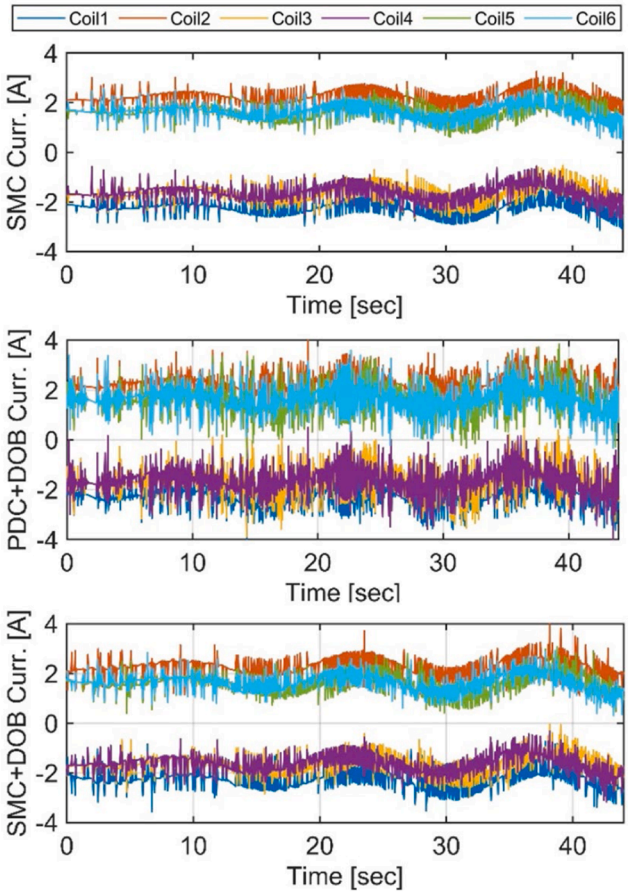

Fig. 9. Applied current in motion control experiments.

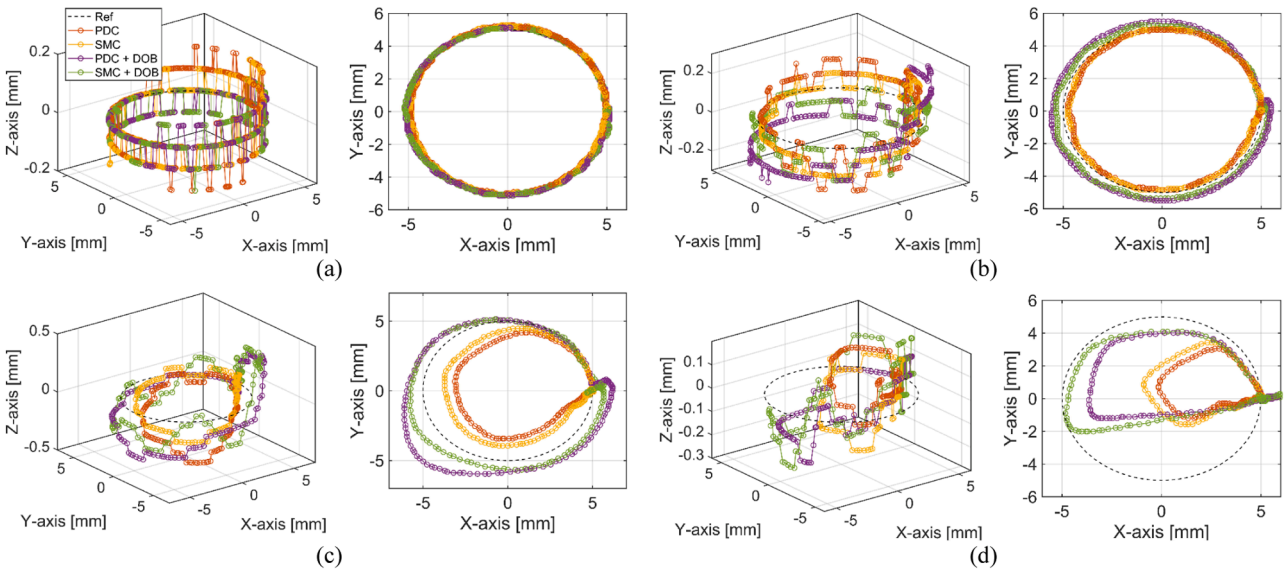

Fig. 10. Experimental results for speed control along a circular trajectory with different set speeds. (a)–(d) Set speed by doubling the difference from (a) min 1.4 mm/s to (d) max 11.4 mm/s.

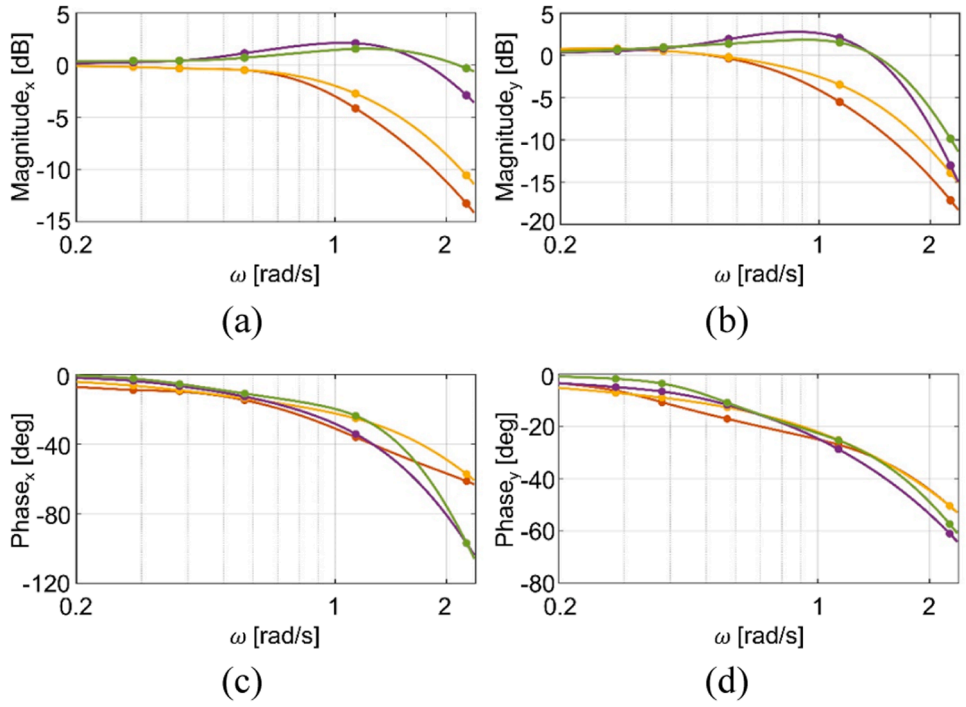

Fig. 11. Analysis of experimental results for circular trajectories in the frequency domain. (a), (b) Magnitude and (c), (d) phase variation.

bances in various research. It involves two key components: equivalent control and switching control law. The general SMC for outer-loop control is as follows:

$$u_r = u_{eq} + u_{sw} \tag{16}$$

where $u_{eq} \in \mathbb{R}^3$ is the continuous equivalent control and $u_{sw} \in \mathbb{R}^3$ is the discontinuous switching control. In this work, we adopted the PID sliding surface vector $s \in \mathbb{R}^3$ in SMC, which is given by Loucif and Kechida (2020):

$$s = K_1 e + K_2 \int e dt + K_3 \dot{e} \tag{17}$$

where K_1, K_2, and K_3 are scalar sliding surface gains, and the tracking error $e \in \mathbb{R}^3$ is defined as $e = x_r - x$, $\dot{e} = \dot{x}_r - \dot{x}$, and $\ddot{e} = \ddot{x}_r - \ddot{x}$. By replacing $\ddot{x}$ with Eq. (10), the time derivative of the sliding surface is expressed as

$$\begin{aligned} \dot{s} &= K_1 \dot{e} + K_2 e + K_3 \ddot{e} \\ &= K_1 \dot{e} + K_2 e + K_3 \left(\ddot{x}_r - m^{-1} (\overline{C} + u_r - \widehat{d} + d) \right) \end{aligned} \tag{18}$$

where $-\widehat{d} + d$ is an unknown term, compensated through switching control. Considering $\dot{s} = 0$ and ideal nominal models, i.e., $d = \widehat{d}$, equivalent control u_{eq} is defined as

Table 2
Comparison of controllers for EMA.

Metric	Ongaro *et al.* (2019)	Ma et al. (2017)	Yang *et al.* (2021)	Lu *et al.* (2022)	Proposed
Controller	PID	Robust control High-gain observer	DOB + Fuzzy logic	ESO + SMC	DOB + SMC
Target object	Sphere $R = 350\ \mu$m	Sphere $R = 10\ \mu$m	Cylinder $R = 450\ \mu$m L = 900 μm	Sphere $R = 150\ \mu$m	Cube 500 μm
Position error / Max velocity	112 μm (RMSE) / 208 μm/s	2.9 μm (RMSE) / 65 μm/s	1210 μm (Avg.) / Approx. 5 mm/s	14.85 μm (RMSE) / Approx. 24 μm/s	400 μm (RMSE) / 11.4 mm/s
Speed analysis	–	–	- Control experiments across various speeds	–	- Control experiments across various speeds
Advantages	- Independent control of two microrobots - Robustness to nonlinearity using force-current mapping	- Provision of robustness and high precision - Reduction of noise measurement using an observer	- Large workspace capability - Handling of disturbances using DOB and fuzzy logic	- Robustness to dynamic disturbances in tracking control	- Simplified controller structure with reduced input chattering - Application to fast dynamic systems
Disadvantages	- High power consumption - High computational cost of the control system	- Complex controller configuration - Limited to small workspaces	- Time-consuming process for generating fuzzy logic rules and tuning gains	- Experimentation constraints in a 2-D environment - Requirement for multiple tuning gains	- Challenges in complex trajectory and various environments

$$u_{eq} = mK_3^{-1}(K_1\dot{e} + K_2 e) + m\ddot{x}_r - \overline{C} \tag{19}$$

And, switching control u_{sw} is constructed as follows:

$$u_{sw} = K_4 \mathrm{sgn}(s) \text{ and } \mathrm{sgn}(s) = \begin{cases} 1 & if \quad s_j > 0 \\ 0 & if \quad s_j = 0 \\ -1 & if \quad s_j < 0 \end{cases} \tag{20}$$

where K_4 is a scalar switching gain, and $\mathrm{sgn}(s)$ represents the component-wise sign function of the vector component s_j, with $j \in \{x, y, z\}$. Applying Eq. (19) and Eq. (20), the final SMC input is rewritten as

$$\begin{aligned} u_r &= u_{eq} + u_{sw} \\ &= mK_3^{-1}(K_1\dot{e} + K_2 e) + m\ddot{x}_r - \overline{C} + K_4 \mathrm{sgn}(s) \end{aligned} \tag{21}$$

3.3. Inner-loop stability analysis

To confirm the stability of the inner-loop, we define the dynamics in the coordinates $(\tilde{p},\ r) = (\eta^{-1}(p - \dot{x}),\ r)$. Then, the signal $\ddot{x}$ in Eq. (6) replacing Eq. (15) is converted as follows:

$$\begin{aligned} \ddot{x} &= m^{-1}(C + u_c + F_d) \\ &= W_p\tilde{p} + m^{-1}(r + C + \overline{C} + u_r + F_d) \end{aligned} \tag{22}$$

The dynamics of the inner-loop system with respect to coordinates of $(\tilde{p},\ r)$ can be obtained by

$$\begin{cases} \eta\dot{\tilde{p}} = -2W_p\tilde{p} - m^{-1}(r + C + \overline{C} + u_r + F_d) \\ \eta\dot{r} = mW_rW_p\tilde{p} + W_r(\overline{C} + u_r) \end{cases} \tag{23}$$

Here, if η is a sufficiently small parameter, the dynamics of Eq. (22) can be considered in the form of standard singular perturbation. In this case, $(\tilde{p},\ r)$ are fast variables, and $(s, e, \dot{e}, u_r, F_d)$ become slow variables. Under certain stability conditions where η is small, the fast variables converge to quasi-steady states $\tilde{p}^*$ and r^*, which corresponds to the equilibrium of fast dynamics, where slow variables remain constant (Ha & Back, 2018; Khalil, 2015).

Therefore, using $\eta = 0$, we can obtain $\tilde{p}^*$ and r^* as follows:

$$\begin{cases} \tilde{p}^* = -m^{-1}W_p^{-1}(\overline{C} + u_r) \\ r^* = \overline{C} - C + u_r - F_d \end{cases} \tag{24}$$

Let define $\psi = [\hat{\tilde{p}}; \hat{r}]$ and $\psi^* = [\tilde{p}^*; r^*]$ where $\hat{\tilde{p}} = \tilde{p} - \tilde{p}^*$ and $\hat{r} = r - r^*$. Considering Eq. (23) and Eq. (24), the dynamics Eq. (23) are reorganized as follows:

$$\eta\dot{\psi} = A_\psi\psi - \eta\dot{\psi}^* \tag{25}$$

where $A_\psi = \begin{bmatrix} -2W_p & -m^{-1}I_n \\ mW_rW_p & 0 \end{bmatrix}$ with $I_n = \mathrm{diag}(1,1,1) \in \mathbb{R}^{3\times 3}$.

To evaluate the stability of the proposed inner-loop system, the Lyapunov function candidate V_{DOB} is given by

$$V_{DOB} = \psi^T P_\psi \psi \tag{26}$$

where P_ψ is a solution of $A_\psi^T P_\psi + P_\psi A_\psi = -Q_\psi$, where A_ψ is a Hurwitz matrix and Q_ψ is a positive definite matrix. Then, the derivative of Lyapunov function is computed as

$$\begin{aligned} \dot{V}_{DOB} &= -2\psi^T P_\psi \dot{\psi}^* + \frac{1}{\eta}\psi^T(A_\psi^T P_\psi + P_\psi A_\psi)\psi \\ &= -2\psi^T P_\psi \dot{\psi}^* - \frac{1}{\eta}\psi^T Q_\psi \psi \\ &\le \kappa_1 \| \psi \| - \frac{1}{\eta}\kappa_2 \| \psi \|^2 \end{aligned} \tag{27}$$

where $\kappa_1 = \max \| 2P_\psi\dot{\psi}^* \|$ and $\kappa_2 = \lambda_{min}(Q_\psi)$. Note that $\lambda_{min}(Q)$ is the minimum eigenvalue of Q. Choosing the parameter η to be sufficiently small value can make $\dot{V}_{DOB} \le 0$ holds so that the stability of the inner-loop can be guaranteed.

3.4. Overall stability analysis

To verify the stability of the overall control system, considering the defined sliding surface Eq. (18) and Eq. (22), its derivative can be obtained as:

$$\dot{s} = K_1\dot{e} + K_2 e + K_3\left(\ddot{x}_r - W_p\tilde{p}\right) - m^{-1}K_3(r + C + \overline{C} + u_r + F_d) \tag{28}$$

Then, replacing u_r with SMC Eq. (21), the dynamics of Eq. (28) is reconstructed in coordinates $(s,\ \tilde{p})$ as follows:

$$\dot{s} = -K_3K_4m^{-1}\mathrm{sgn}(s) - K_3W_p\tilde{p} \tag{29}$$

To prove the stability of the overall control system, the Lyapunov function candidate $V_{overall}$ can be chosen as (Li et al., 2012)

$$V_{overall} = V_{DOB} + V_{SMC} = \psi^T P_\psi \psi + \frac{1}{2}s^T s \tag{30}$$

where V_{SMC} is the Lyapunov function of SMC. Then, the time derivative of V_{SMC} is derived as follows:

$$\begin{aligned}\dot{V}_{SMC} &= s^T\dot{s} \\ &= -s^T\left(K_3K_4m^{-1}\mathrm{sgn}(s) + K_3W_p\tilde{p}\right) \\ &= -s^T(\kappa_3\mathrm{sgn}(s) + \kappa_4)\end{aligned} \tag{31}$$

where $\kappa_3 = K_3K_4m^{-1}$ and $\kappa_4 = K_3W_p\tilde{p}$. If $\kappa_3 > \sup\| \kappa_4 \|$ can be obtained through tuning of K_3 and K_4, then Eq. (30) guarantees that $\dot{V}_{SMC} = s^T\dot{s} \leq 0$, ensuring the stability of the SMC.

Finally, if η is chosen sufficiently small to guarantee $\dot{V}_{DOB} \leq 0$, thereby ensuring the stability of the inner-loop, and $\kappa_3 > \sup\| \kappa_4 \|$, the stability of the overall system is established, i.e., the overall control system is bounded and satisfies the following condition Eq. (7).

4. Simulation analysis

In this section, we evaluate the performance of the proposed controller through simulations and experiments. Before implementing the controller in a real system, the performances of DOB and SMC were analyzed on simulations. By tuning the parameters of DOB and SMC, we investigated the effect of tuning gains on the controller performance. Subsequently, two experiments were conducted through a tracking-based manipulation test and a speed-control test with the magnetic object. Then, we analyzed the results in the time and frequency domains to validate the proposed controller by comparing it with other controllers.

Simulations of DOB were conducted to establish a relationship between robustness and sensitivity with observer parameter variation. The responses of the sensitivity function defined as a transfer function of the magnetic force against disturbance were analyzed from numerical simulations (Sariyildiz et al., 2020). Fig. 4(a) shows the results of the sensitivity function of the DOB in the frequency domain. We tuned the gains (η, α, β) of the designed LPF; α and β are the arbitrary matrix elements of $W_p = \mathrm{diag}(\alpha_x,\ \alpha_y,\ \alpha_z)$ and $W_r = \mathrm{diag}\left(\beta_x,\ \beta_y,\ \beta_z\right)$. When η was set to a small value or β was set to a large value, the broadened bandwidth of LPF was observed indicating that the robustness of the DOB could be improved through appropriate disturbance compensation. However, parameter determination with high values widens the bandwidth excessively which can cause a waterbed effect between robustness and sensitivity, which occurs when β is increased as shown in Fig. 4(a). Simulation results of disturbance estimation in the time domain are illustrated in Fig. 4(b). For simulation purposes, it was assumed that the disturbance was a mixed signal of 100 and 200 Hz sinewave with virtual noise. The results show that the gain η decides the performance of the DOB, i.e., smaller values of gain (η) can induce a higher accuracy of disturbance estimation; however, it shows a lower capability for noise filtering. Theoretically, a controller designed using DOB is a two-degree-of-freedom controller, so it has characteristics that can achieve performance and stability independently (Sariyildiz & Ohnishi, 2014). For example, for a system with large uncertainties, stability can be ensured by choosing a sufficiently small η. However, because the real system is easily affected by noise and the actuator bandwidth is inherently limited, output instability may occur if η is too small; this characteristic can be confirmed in Fig. 4(b).

Simulations of the proposed controller were performed to validate the motion control capability. The plant model was constructed by extracting magnetic field functions for position and current obtained through FEA simulation (see Fig. 2), and Eq. (5) was used for the object dynamics. Additionally, it was assumed that the lump disturbance in the model arises from uncertainty in the plant model and high-frequency noise added by simulating the actual experimental environment. The reference trajectory was selected as a 3-D helical path, and the control performances of the proposed DOB-based SMC, conventional SMC, and a proportional derivative controller (PDC) were compared. Fig. 5 shows the results of position control when using attempted controllers. PDC shows that steady-state errors exist for each axis, and SMC improves driving performance through switching inputs including an internal integral term. The larger the gain of the switching input (Fig. 7), the faster the output converges to the reference path, resulting in a decrease in steady-state error. In the case of SMC-gain$_1$, the switching input in a specific direction is continuously maintained to compensate for the tracking error in the biased signal direction. However, the switching gain is insufficient to compensate for the disturbance caused by the model uncertainty, resulting in the steady-state error. SMC-gain$_2$, which uses a higher switching gain, makes it easier to compensate for the tracking error but introduces chattering in the input signal. This illustrates a tradeoff: as the switching gain increases, compensation becomes more effective, but chattering also intensifies. For instance, when the input switches along the z-axis in a simulation, excessive values can cause instantaneous errors to increase. While this might be acceptable in an ideal system, it cannot guarantee output performance and stability against unexpected disturbances in practical scenarios. The proposed DOB-based SMC recorded the smallest error in Fig. 6 and achieved reduced chattering amplification compared to SMC gains despite the low gain of the switching input in Fig. 7. This indicates that the expansion of the bandwidth of LPF due to over-tuning of η, the gain of DOB, can be prevented by SMC, and the resulting noise sensitivity can be reduced. As a result, the proposed controller achieved more accurate and faster tracking performance than the previously mentioned controllers while confirming both position and speed control possibilities.

5. Experimental verification

5.1. Experimental setup

A magnetic cuboid object with a side length of 500 μm was used as a target magnetic robot, and the experiments were conducted in an acrylic box filled with silicone oil as the medium in the system ROI as shown in Fig. 1. The environment was set up static conditions with no flow inside the medium. Control input magnitude and the rate are constrained depending on the EMA system and power supply performance. Here, the input current is limited by 10 A and the control frequency is limited by 20 Hz. Two Microsoft LifeCam (Microsoft, USA) were placed in the xy- and xz-planes to track the position of the object in real time. LabVIEW (National Instrument, USA) and MATLAB (MathWorks, USA) scripts were used to implement the program.

To implement the proposed controller in the actual system, parameter tuning was conducted following these guidelines: the process begins with tuning the outer-loop controller (SMC) and is followed by tuning the inner-loop operator (DOB). The initial sliding surface parameters (K_1,K_2,K_3, and K_4) are selected based on tracking control simulation results, after which minor tuning is performed iteratively through repeated experiments. Once SMC performance reaches saturation, the DOB gain (η) is tuned. Major tuning is performed based on factors such as noise sensitivity and control precision, followed by fine-tuning through additional experiments.

Two experiments were conducted for validation: (1) a tracking position control test and (2) a speed control test in comparison with other controllers. In detail, the first test verified the ability to control position and velocity along a reference path with increasing setpoints from the starting point. The second test was conducted for speed control experiments by increasing the set point interval so that the average speed of the reference circular path was doubled. The maintenance of control performance according to set speed and resistance to off-course motion accompanying fast dynamics was evaluated. For comparative evaluation, the performance of four controllers, including the proposed controller (DOB-based SMC), was evaluated along the same trajectories. The comparative controllers include PDC, SMC, and DOB-based PDC, with the control gains tuned through repeated experiments under consistent conditions.

5.2. Position control

The tracking control results are presented in Fig. 8, and the errors corresponding to each axis are shown in Fig. 8(b). The position error of RMSE ± STD (root mean square error ± standard deviation) for the controller was measured. The errors of each controller are depicted in Table 1. Compared to the PDC, the proposed controller showed a performance improvement of approximately 71 %. Furthermore, the real-time velocity change trends are shown in Fig. 8(c). The results of the error and velocity change proved that the proposed controller combined with SMC and DOB exhibited faster convergence speed and compensation ability against unpredictable disturbances. In particular, the driving performance was dominated by the influence of DOB and the gain η that operated it. However, when simply using DOB and PDC, chattering problems occurred in the input current because both the estimation and compensation of the disturbance were allotted only to the gain η. This problem can be mitigated by dividing the gain influence of each operator through a combination of SMC and DOB. In particular, it can be observed that the input current of DOB-based SMC alleviated the chattering problem more than the DOB-based PDC current which recorded a similar error (see Fig. 9). The tracking control test results correspond to object control with slow dynamics, and then a speed control test was performed to evaluate robustness and controllability against inputs that cause fast dynamic and nonlinear characteristics.

5.3. Speed control

Fig. 10 presents the results of speed-control performance. The set speeds correspond to 1.43, 2.86, 5.71, and 11.42 mm/s in Fig. 10(a)–(d), respectively, and the controller gains used for the previous tracking motion control were used. The experiment was conducted along a path in which the object rotated counterclockwise, and the task was set to end when the starting point was reached. At a low speed, all controllers showed effective compensation ability, and the performance gradually decreased as the setting speed increased. Here, SMC had a compensating effect compared to PDC, but it did not affect significantly on a fast-moving actuator with a fixed gain. Specifically, as the speed increases, the gain of the SMC should increase; however, the SMC does not serve as an appropriate compensator because it causes chattering problems owing to switching input and instability in a steady state. By contrast, DOB was more effective than SMC in compensating for system errors that increased with speed, even though there were cases of excessive error correction in high-speed experiments. In Fig. 10(c), it is the speed section where the performance of DOB-based SMC differs compared to the DOB-based PDC result, and the robustness of SMC against excessive disturbance estimation of DOB can be confirmed. Fig. 10(d) is a section where the collapse of motion is noticeable, and the resistance of the proposed controller can be seen.

These results can confirm the efficacy of the proposed control scheme more closely from the magnitude and phase shift results according to the angular velocity of the object in the frequency domain as shown in Fig. 11. They show the magnitude change with respect to angular velocity changes. Because of the initial position of the object and the accumulated error during driving, the magnitude on the y-axis was measured lower than that on the x-axis at high speeds. Nevertheless, when using the proposed controller, the x-axis magnitude showed a low reduction result within 5 dB, which proves that it is relatively superior to the conventional controller in terms of speed control.

6. Conclusion

In this paper, we proposed a double-loop robust controller composed of SMC and DOB to enhance the position and speed control performances in the wireless manipulation of a magnetic object using an EMA. The controller was designed to estimate and compensate for lump disturbances caused by model uncertainty, nonlinearity, and external effects. The relationship between the controller parameters and the EMA performance was investigated and the stability of the system was analyzed on this basis. To evaluate the performance of the proposed controller, simulations and experiments were conducted on a magnetic object. The results demonstrated that position control accuracy reached 0.4 mm at a rated speed within 1 mm/s, showing a 71 % improvement compared to PD control. Additionally, the speed control performance of the magnetic object was evaluated, achieving a maximum speed of 11.4 mm/s, which demonstrated relatively effective adaptability compared to other control approaches. Notably, a detailed comparative analysis of the proposed controller, alongside reported controllers, is summarized, highlighting their advantages and disadvantages (see Appendix A).

The main contributions of this study are as follows: First, we developed a double-loop control structure that combines SMC and DOB to enhance the robustness of the EMA system against nonlinearities and unmodeled parameters. By incorporating linearized approximations and several key assumptions, the proposed approach addressed a balance between simplicity and practicality, while effectively addressing the inherent complexities of the EMA system. This controller ensures stable performance and mitigates the chattering issue associated with input currents. Second, we analyzed the designed parameters of the controller with consideration of stability analysis and its impact on the output. The controller consists of a relatively simple structure with limited parameter gains (K_1, K_2, K_3, K_4, and η). The correlation between these parameters and the EMA system output was analyzed through simulation, and the practical effectiveness of each operator was validated. Third, the applicability of the proposed controller for speed control was thoroughly evaluated. Unlike previous studies that primarily focused on position control within a limited speed range, this study conducted experiments under both low-speed and high-speed conditions. The results show that the proposed controller enhances control performance at higher input speeds and extends the critical speed threshold beyond which off-course motion occurs. Notably, this study is the first to investigate speed control in EMA systems, providing a detailed analysis of off-course motion under varying speed conditions and demonstrating the controller's effectiveness in addressing dynamic operational challenges.

Nevertheless, challenges remain in implementing speed-control technology for EMA systems, particularly in achieving appropriate gain tuning. While the proposed controller has demonstrated its capability in speed control; however, effectively compensating for unpredictable motion errors with minimal fluctuations in real-time is still difficult. This means that the system may need adaptive gain tuning mechanisms rather than relying on fixed gain values. Furthermore, data-driven learning approaches could offer potential improvements in enhancing system adaptability and performance.

Future works will focus on expanding the applicability of the proposed control system to diverse operational conditions, including those involving complex trajectories, fluid flow dynamics, and other external disturbances. Comprehensive analysis and experimental validation will be conducted to further enhance the robustness and adaptability of the system. These advancements are expected to enable a wide range of applications, such as capsule endoscopes, needles, catheters, and microrobots in the biomedical field.

CRediT authorship contribution statement

Han-Sol Lee: Writing – original draft, Visualization, Validation, Software, Methodology, Investigation. **Yeongoh Ko:** Validation, Formal analysis, Data curation. **Juhoon Back:** Writing – original draft, Validation, Methodology. **Keum-Shik Hong:** Validation, Supervision, Resources. **Chang-Sei Kim:** Writing – review & editing, Validation, Supervision, Funding acquisition, Conceptualization.

Declaration of competing interest

The authors declare that they have no known competing financial

interests or personal relationships that could have appeared to influence the work reported in this paper.

Acknowledgements

This work was supported by National Research Foundation of Korea (NRF) grant funded by the Korea government (MSIT) (No. 2023R1A2C2003086) and by the Ministry of Trade, Industry and Energy (MOTIE), Korea, under the "Global Industrial Technology Cooperation Center (GITCC) program" supervised by the Korea Institute for Advancement of Technology (KIAT).(Task No P0028454).

Appendix A. Comparison of EMA controllers

See Table 2.

References

Bailey, A. B. (1974). Sphere drag coefficient for subsonic speeds in continuum and free-molecule flows. *Journal of Fluid Mechanics, 65*(2), 401–410. https://doi.org/10.1017/S0022112074001443

Cai, M., Qi, Z., Cao, Y., Wu, X., Xu, T., & Zhang, L. (2024). Development of reconfigurable electromagnetic actuation system with large workspaces: Design, optimization, and validation. *IEEE Transactions on Automation Science and Engineering*, 1–12. https://doi.org/10.1109/tase.2024.3435035. *PP*.

Cao, H., Xing, L., Mo, H., Li, D., & Sun, D. (2022). Image-guided corridor-based motion planning and magnetic control of microrotor in dynamic environments. *IEEE/ASME Transactions on Mechatronics, 27*(6), 5415–5426. https://doi.org/10.1109/TMECH.2022.3181588

Chen, J., Zhao, C., Tang, Q., Liu, X., Wang, Z., Tan, C., et al. (2023). Low chattering trajectory tracking control of non-singular fast terminal sliding mode based on disturbance observer. *International Journal of Control, Automation and Systems, 21*(2), 440–451. https://doi.org/10.1007/s12555-021-0604-0

Chen, R., Folio, D., & Ferreira, A. (2021). Mathematical approach for the design configuration of magnetic system with multiple electromagnets. *Robotics and Autonomous Systems, 135*, Article 103674. https://doi.org/10.1016/j.robot.2020.103674

Fu, S., Chen, B., Li, D., Han, J., Xu, S., Wang, S., et al. (2023). A magnetically controlled guidewire robot system with steering and propulsion capabilities for vascular interventional surgery. *Advanced Intelligent Systems, 5*(11). https://doi.org/10.1002/aisy.202300267

Gervasoni, S., Pedrini, N., Rifai, T., Fischer, C., Landers, F. C., Mattmann, M., et al. (2024). A Human-scale clinically ready electromagnetic navigation system for magnetically responsive biomaterials and medical devices. *Advanced Materials, 36*(31), 1–20. https://doi.org/10.1002/adma.202310701

Gharamaleki, N. L., Kim, D., Lee, G., Kim, J. Y., & Choi, H. (2024). Magnetic field control using an electromagnetic actuation system with combined air-core and metal-core coils. *Advanced Intelligent Systems*. , Article 2400462. https://doi.org/10.1002/aisy.202400462

Go, G., Jeong, S. G., Yoo, A., Han, J., Kang, B., Kim, S., et al. (2020). Human adipose-derived mesenchymal stem cell-based medical microrobot system for knee cartilage regeneration in vivo. *Science Robotics, 5*(38). https://doi.org/10.1126/scirobotics.aay6626

Griffiths, D. J. (2017). *Introduction to electrodynamics* (4th ed.). Pearson. *Pearson*.

Ha, W., & Back, J. (2018). A disturbance observer-based robust tracking controller for uncertain robot manipulators. *International Journal of Control, Automation and Systems, 16*(2), 417–425. https://doi.org/10.1007/s12555-017-0188-x

Hashemi, E., Khajepour, A., Moshchuk, N., & Chen, S. K. (2022). Real-time road bank estimation with disturbance observers for vehicle control systems. *IEEE Transactions on Control Systems Technology, 30*(1), 443–450. https://doi.org/10.1109/TCST.2021.3062384

Hu, W., Lum, G. Z., Mastrangeli, M., & Sitti, M. (2018). Small-scale soft-bodied robot with multimodal locomotion. *Nature, 554*(7690), 81–85. https://doi.org/10.1038/nature25443

Huang, Z., Li, Y., Wei, T., Lu, D., Shi, C., & Hu, C. (2024). Enhanced localization strategy for magnetic capsule robot using on-board nine-axis IMU through incorporation of alternating magnetic field. *IEEE Transactions on Instrumentation and Measurement, 73*, 1–12. https://doi.org/10.1109/TIM.2024.3350144

Khalil, H. K. (2015). *Nonlinear control* (Global edition). PEARSON.

Ko, Y., Lee, H. S., & Kim, C. S. (2024). Model-based real-time simulator for robotic electromagnetic actuation. *IEEE Robotics and Automation Letters, 9*(4), 3870–3877.

Kummer, M. P., Abbott, J. J., Kratochvil, B. E., Borer, R., Sengul, A., & Nelson, B. J. (2010). OctoMag: An electromagnetic system for 5-DOF wireless micromanipulation. *IEEE Transactions on Robotics, 26*(6), 1006–1017. https://doi.org/10.1109/TRO.2010.2073030

Law, J., Du, X., Tang, W., Yu, J., & Sun, Y. (2024). Navigation of magnetic microrobotic swarms with maintained structural integrity in fluidic flow. *IEEE/ASME Transactions on Mechatronics, 29*(1), 74–84. https://doi.org/10.1109/TMECH.2023.3269600

Lee, H. S., Back, J., & Kim, C. S. (2024). Disturbance observer-based robust controller for a multiple-electromagnets actuator. *IEEE Transactions on Industrial Electronics, 71*(1), 901–911. https://doi.org/10.1109/TIE.2023.3247740

Li, D., Dong, D., Lam, W., Xing, L., Wei, T., & Sun, D. (2020). Automated in vivo navigation of magnetic-driven microrobots using OCT imaging feedback. *IEEE Transactions on Biomedical Engineering, 67*(8), 2349–2358. https://doi.org/10.1109/TBME.2019.2960530

Li, Y., Zheng, Q., & Yang, L. (2012). Design of robust sliding mode control with disturbance observer for multi-axis coordinated traveling system. *Computers and Mathematics with Applications, 64*(5), 759–765. https://doi.org/10.1016/j.camwa.2011.11.053

Loucif, F., & Kechida, S. (2020). Optimization of sliding mode control with PID surface for robot manipulator by evolutionary algorithms. *Open Computer Science, 10*(1), 369–407. https://doi.org/10.1515/comp-2020-0144

Lu, H., Zhang, M., Yang, Y., Huang, Q., Fukuda, T., Wang, Z., et al. (2018). A bioinspired multilegged soft millirobot that functions in both dry and wet conditions. *Nature Communications, 9*(1). https://doi.org/10.1038/s41467-018-06491-9

Lu, J., Liu, Y., Huang, W., Bi, K., Zhu, Y., & Fan, Q. (2022). Robust control strategy of gradient magnetic drive for microrobots based on extended State observer. *Cyborg and Bionic Systems, 2022*. https://doi.org/10.34133/2022/9835014

Ma, W., Li, J., Niu, F., Ji, H., & Sun, D. (2017). Robust control to manipulate a microparticle with electromagnetic coil system. *IEEE Transactions on Industrial Electronics, 64*(11), 8566–8577. https://doi.org/10.1109/TIE.2017.2701759

Marino, H., Bergeles, C., & Nelson, B. J. (2014). Robust electromagnetic control of microrobots under force and localization uncertainties. *IEEE Transactions on Automation Science and Engineering, 11*(1), 310–316. https://doi.org/10.1109/TASE.2013.2265135

Mechali, O., Xu, L., Xie, X., & Iqbal, J. (2022). Theory and practice for autonomous formation flight of quadrotors via distributed robust sliding mode control protocol with fixed-time stability guarantee. *Control Engineering Practice, 123*. https://doi.org/10.1016/j.conengprac.2022.105150

Nguyen, K. T., Go, G., Zhen, J., Hoang, M. C., Kang, B., Choi, E., et al. (2021). Locomotion and disaggregation control of paramagnetic nanoclusters using wireless electromagnetic fields for enhanced targeted drug delivery. *Scientific Reports, 11*(1), 1–13. https://doi.org/10.1038/s41598-021-94446-4

Ongaro, F., Pane, S., Scheggi, S., & Misra, S. (2019). Design of an electromagnetic setup for independent three-dimensional control of pairs of identical and nonidentical microrobots. *IEEE Transactions on Robotics, 35*(1), 174–183. https://doi.org/10.1109/TRO.2018.2875393

Ovalle, L., Ríos, H., Llama, M., Santibáñez, V., & Dzul, A. (2019). Omnidirectional mobile robot robust tracking: Sliding-mode output-based control approaches. *Control Engineering Practice, 85*, 50–58. https://doi.org/10.1016/j.conengprac.2019.01.002

Peker, F., Beşer, M. A., Işlldar, E., Terzioğlu, Y., Erten, A. C., Kumbasar, T., et al. (2024). Towards capsule endoscope locomotion in large volumes: Design, fuzzy modeling, and testing. *Robotica, 42*(1), 203–224. https://doi.org/10.1017/S026357472300142X

Sariyildiz, E., Oboe, R., & Ohnishi, K. (2020). Disturbance observer-based robust control and its applications: 35th anniversary overview. *IEEE Transactions on Industrial Electronics, 67*(3), 2042–2053. https://doi.org/10.1109/TIE.2019.2903752

Sariyildiz, E., & Ohnishi, K. (2014). A guide to design disturbance observer. *Journal of Dynamic Systems, Measurement and Control, Transactions of the ASME, 136*(2). https://doi.org/10.1115/1.4025801

Sikorski, J., Heunis, C. M., Franco, F., & Misra, S. (2019). The ARMM System: An optimized mobile electromagnetic coil for non-linear actuation of flexible surgical instruments. *IEEE Transactions on Magnetics, 55*(9), 1–9. https://doi.org/10.1109/tmag.2019.2917370

Song, L., Dai, Y., Wang, L., Zhang, W., Ji, Y., Cao, Y., et al. (2022). Motion control of capsule robot based on adaptive magnetic levitation using electromagnetic coil. *IEEE Transactions on Automation Science and Engineering*, 1–12. https://doi.org/10.1109/TASE.2022.3201966

Wang, Q., Zhang, J., Yu, J., Lang, J., Lyu, Z., Chen, Y., et al. (2023a). Untethered small-scale machines for microrobotic manipulation: From individual and multiple to collective machines. *ACS nano, 17*(14), 13081–13109. https://doi.org/10.1021/acsnano.3c05328

Wang, Z., Klingner, A., Magdanz, V., Misra, S., & Khalil, I. S. M. (2023b). Soft bio-microrobots: Toward biomedical applications. *Advanced Intelligent Systems*. https://doi.org/10.1002/aisy.202300093

Yang, Z., Yang, L., & Zhang, L. (2021). Autonomous navigation of magnetic microrobots in A large workspace using mobile-coil system. *IEEE/ASME Transactions on Mechatronics*. https://doi.org/10.1109/TMECH.2021.3054927

Yang, Z., & Zhang, L. (2020). Magnetic actuation Systems for Miniature robots: A review. *Advanced Intelligent Systems, 2*(9), Article 2000082. https://doi.org/10.1002/aisy.202000082

Zhang, H., Li, Y., Shi, X., Sun, Y., Li, J., Huang, Y., et al. (2024). Toward automatic stomach screening using a wireless magnetically actuated capsule endoscope. *IEEE Transactions on Medical Robotics and Bionics, 6*(2), 512–523. https://doi.org/10.1109/TMRB.2024.3387040

Zhong, Q., Fang, X., Ding, Z., & Liu, F. (2023). Robust control of manned submersible vehicle with nonlinear MPC and disturbance observer. *IEEE/CAA Journal of Automatica Sinica, 10*(5), 1349–1351. https://doi.org/10.1109/JAS.2023.123429